Article

Dynamic Monitoring of the Standard Penetration of PHC Tubular Piles and Analysis of the Construction Effect Based on Monocular Visual Digital Photography

Guojian Zhang [1,2,3,*], Zhiyong Liu [1], Wei Xiong [4], Sifeng Zhang [5,*], Shengzhen Liu [6], Zhiwei Wang [1] and Yushuai Wang [5]

1   School of Surveying and Geo-Informatics, Shandong Jianzhu University, Jinan 250101, China
2   China & Post-Doctoral Workstation of Technology Research Institute in Shandong Energy Group Co., Ltd., Jinan 250101, China
3   School of Environmental Science and Spatial Informatics, China University of Mining and Technology, Daxue Road 1, Xuzhou 221116, China
4   Shandong Road and Bridge Engineering Design Consulting Co., Ltd., Jinan 250014, China
5   School of Transportation Engineering, Shandong Jianzhu University, Jinan 250101, China
6   First Geodetic Survey Team of Natural Resources Department, Xi'an 710054, China
*   Correspondence: g_j_zhang@cumt.edu.cn (G.Z.); sddxzsf@sdjzu.edu.cn (S.Z.); Tel.: +86-187-64018326 (G.Z.); +86-135-73109817 (S.Z.)

Abstract: The penetration of large-diameter tubular piles and their relevant construction effect have significant influences on the bearing capacity of piles and nearby buildings (structures). This study focuses on developing an indoor test model device for the dynamic field monitoring of the construction effect of penetrated large-diameter tubular piles based on monocular visual digital photography. The results show that the relationship between the penetration of the tubular piles and time function (blow counts) changes from a logarithmic function to a linear function when piles penetrate from the loose layer to the sandy layer, and then to the silty soil layer. The penetration rates differ significantly under different formation conditions. There are obvious plugging and squeezing effects as tubular piles penetrate different strata. The plugging effect radiates outward in a rectangular shape. The influence sphere of the squeezing effect is divided into the shear failure zone, radial squeezing zone, and hemispherical expansion zone. According to the measurement data, the squeezing effect increases first and then weakens during the construction of tubular piles. This makes the adjacent pile deviate from the initial position by 17.4 mm, making the next pile deviate from the initial position by 6.4 mm, to the maximum extent. This further verifies the superiority of pile-jumping construction. The research conclusions can provide reasonable suggestions and a reference basis to improve the penetration parameters of tubular piles and optimise their construction techniques.

Keywords: PHC tubular piles; close-range photogrammetry; penetration; construction effect; dynamic monitoring

1. Introduction

When reinforcing soft soil foundations using tubular piles, their penetration and relevant construction effects could influence the resistance against pile settlement and the failure mode and bearing capacity of the piles. Therefore, these effects have a significant influence on the bearing capacity of the composite foundation [1].

Currently, the dial indicator contact measuring method, static load testers, tile marking measuring method, inclinometer measuring method, and accelerometer measuring method are commonly used to monitor the penetration of tubular piles. For example, Xing H.F. et al. analysed the pile settlement laws of PHC tubular piles by determining the blow counts of settled piles, further optimising the penetration design of tubular piles through the incorporation of geological exploration data [2]. Further, Luo C.L. et al. simulated real

piles by using square steel bars and marked scales on the bars to measure the penetration depths of the piles [3].

Studies on the construction effect of large-diameter tubular piles mainly focus on the evolution mechanism and influencing factors of the construction effect and the bearing capacity of pile foundations based on the construction effect. Concerning the evolution mechanism of the construction effect of tubular piles, Lei H.Y. et al. monitored the hyperstatic pore pressure and soil mass displacement through field tests, analysed the squeezing effect of high-rise platform tubular piles in soft soil regions, and determined the dissipation laws of hyperstatic pore water pressure and variation characteristics of soil mass displacement caused by pile settlement [4]. Xie Y.J. et al. carried out statistical analyses on soil plug data during the penetration of 44 PHC piles (60–65 cm) from three sites and five types of typical soft soil foundations in Shanghai. They concluded that the IFR and soil plug ratio (PLR) had a linear relationship. Moreover, the empirical formula was fitted [5]. Xing H.F. et al. analysed the settlement laws of PHC tubular piles by observing the blow counts, finding that PHC tubular piles had a very strong squeezing effect on surrounding soil masses [6]. Yu X. et al. studied the pile–soil interaction of open-ended and closed-ended piles through finite element analysis and determined the stress mechanism of soil plug soils under different vertical loads [7]. Chen L.Z. et al. proposed a calculation formula for the soil plug height based on the Terzaghi theory of ultimate bearing capacity [8]. Liu J.W. et al. studied the influences of tubular pile diameters and other factors on the evolution laws of soil plugs using discrete element numerical simulation software [9].

Concerning the influencing factors of construction effects, Ko J. et al. simulated the piling process of steel tubular piles in sandy soils and explored the influences of the pile diameter, piling energy, and elasticity modulus of soils and bearing strata on the plugging effect. The researchers believed that the piling energy was the primary influencing factor of the plugging effect, followed by the pile diameter, penetration depth into bearing strata, and elasticity modulus of the soil mass [10]. Zhan Y.X. et al. simulated the settlement process of open-ended tubular piles of different models based on the particle flow program PFC2D. They then determined the macro-mechanical response mechanism during settlement by analysing the microscopic changes in the soil mass. The results demonstrated that the diameter of the tubular piles influences the plugging effect significantly. With an increase in this diameter, the plugging effect decreased quickly [11]. Further, Tang B. et al. carried out field penetration tests on 17 groups of open-ended and closed-ended model piles into clays and found that the radius–thickness ratio and diameter of the tubular piles influenced the soil plug height greatly. Moreover, they found a linear relationship between the IFR and soil plug ratio (PLR). Given the same tubular pile, the bearing capacity of open-ended tubular piles was 0.2–0.3 times lower than that of closed-ended ones [12]. Through multiple tests, Leane B.M. et al. found that, given the same foundation, the soil plug height in piles was positively related to the inner diameter and radius–thickness ratio of open-ended tubular piles [13]. Wang T. et al. carried out numerical simulation analyses on the penetration process of tubular piles under the influences of different factors. They concluded that the plugging effect is positively related to the pile–soil friction coefficient. However, it is negatively related to the pile diameter (at the same wall thickness). Overall, the radius–thickness ratio of piles is a decisive factor influencing the soil plug height [14].

Concerning the bearing capacity of pile foundations, Doherty P. et al. conducted a pile pressing test into soft clay to investigate the influences of end conditions on the bearing capacity of tubular piles. They found that the total radial stress during the construction of tubular piles was directly related to excess pore water pressure and the soil plug degree, presenting a linear increase with reductions in the IFR. Fingings revealed that the end resistance on the annual section was independent of the IFR [15]. Gavin F. et al. investigated the influences of pile end conditions and the closing degree of soil plugs on the resistance development of pile bodies, proposing an estimation formula for the vertical bearing capacity of open-ended tubular piles, which could estimate the vertical bearing capacity of tubular piles well [16]. Thongmunee S. et al. discussed the bearing mechanism of dry sand

soil plugs through a tubular pile model loading test and characterised the plugging effect using the DEM model. The results showed that, with increases in the relative soil plug density, the pressing strength on the pile increased. The DEM simulation results agreed well with test results when the pressing strength on the pile was relatively small [17]. Mohammed Y. et al. studied the influences of soil plugs on the bearing capacity and carried out tests on 60 model piles. Results revealed that tubular piles reached the complete soil plug state in loose and medium-density sandy soils during static pressure piling but were in a partial soil plug state in compact sandy soils. The bearing capacity of tubular piles was related to the PLR, and its increase rate in compact sandy soils was higher than that in loose and medium-density sandy soils [18]. Mohammed Y. et al. compared the influences of the soil plug degree on the bearing capacities of single open-ended and closed-ended steel tubular piles, revising 24 open-ended steel tubular pile models. They believed that the ultimate soil plug height was closely related to the piling mode and compactness of strata [19].

In general, common penetration monitoring methods have certain disadvantages, such as being time-consuming, labour-intensive, and difficult to operate. Further, they often have a low measurement accuracy and cannot adequately conduct standard dynamic monitoring of penetration. Moreover, studies on the construction effect of large-diameter tubular piles face issues regarding insufficient field displacement measurement data and visual monitoring data from indoor tests. Therefore, they cannot reflect the entire production process and sphere of influence of the construction effect. Digital photography is used for technological support in this study, given its low cost, high measurement accuracy, and simple operation [20,21].

Therefore, this paper intends to use digital photography technology to monitor the dynamic penetration value and squeezing effect of large-diameter pipe piles on the spot. According to the monitoring results, the relationship between the dynamic penetration value of large-diameter pipe piles, the impact frequency and strata structure is analysed, the evolution law and influence range of squeezing effect is analysed, and laboratory tests are carried out to provide additional explanations.

2. Monocular Visual Digital Photography

2.1. Digital Close-Range Photogrammetry Technology

Digital close-range photogrammetry integrates the close-range photogrammetry technique, image processing technology, and computer technology. It uses a digital camera as the primary monitoring equipment. It can monitor several sites simultaneously and acquire transient deformation information. At present, this technology has been applied successfully to the dynamic deformation monitoring of several objects, such as steel structures [22], bridges [23,24] masonry walls [25], aeroplane wings [26] and large steel-structure buildings [27,28]. Studies on dynamic deformation monitoring using digital close-range photogrammetry technology based on digital cameras are relatively mature. Figure 1 shows the camera in this study.
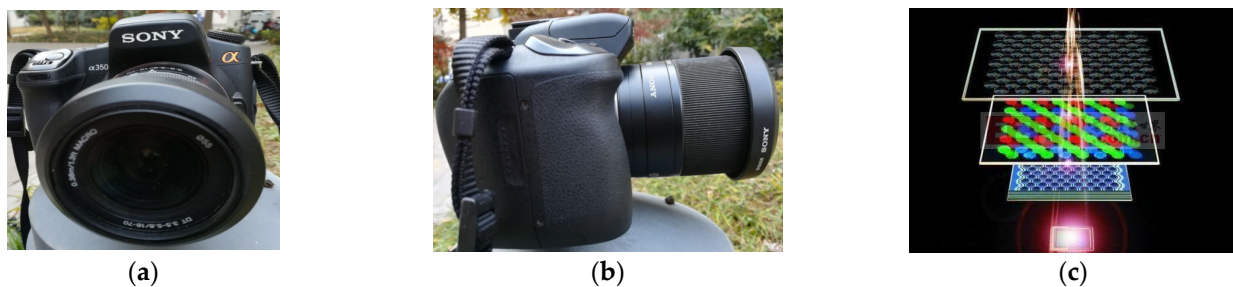

| (a) | (b) | (c) |

Figure 1. A Sony-350 camera was used for the monocular digital photography, displaying (**a**) front view, (**b**) side view, and (**c**) principle of CCD imaging.

2.2. Image-Forming Principle and Calibration of the Camera

The image-forming principle of the digital camera can be expressed using a pinhole imaging model [29–32]. Its details are as follows:

$$sm' = A[R| \, t]M' \tag{1}$$

where (x, y, z) are the three-dimensional coordinates of points in the spatial coordinate system and (μ, ν) are the plane coordinates of the projection points. A is the internal parameter matrix of the camera. (c_x, c_y) are the horizontal and vertical offsets of the shaft, respectively. Finally, (f_x, f_y) are the horizontal and vertical focal lengths of the lens, respectively.

$$S \begin{bmatrix} \mu \\ \nu \\ 1 \end{bmatrix} = \begin{bmatrix} f_x & 0 & c_x \\ 0 & f_y & c_y \\ 0 & 0 & 1 \end{bmatrix} \begin{bmatrix} r_{11} & r_{12} & r_{13} & t_1 \\ r_{21} & r_{22} & r_{23} & t_2 \\ r_{31} & r_{32} & r_{33} & t_3 \end{bmatrix} \begin{bmatrix} X \\ Y \\ Z \\ 1 \end{bmatrix} \tag{2}$$

In previous studies, digital cameras were usually calibrated using the grid method and direct linear transformation method. Although these methods have relatively high accuracy, their calibration efficiency is low. Hence, Zhang's calibration method [33], which is more convenient and quicker, was applied in this study to calibrate smartphone cameras. Concerning the working principle, Zhang's calibration method calculates the internal parameter matrix and distortion coefficients of the camera by using the pinhole imaging model. The process is as follows:

(1) A black-and-white checkerboard was designed. Pictures of the checkerboard were taken using smartphones at different postures, from different distances (Figure 2). A group of pictures was taken, and the poor-quality ones were eliminated. Finally, the calibration results were obtained, as shown in Table 1.

(2) The calibration results were compared with the results of the MATLAB Camera Calibrator, and they had only slight differences. Moreover, the mean reprojection error of the PDMS was smaller than 0.5 pixels.
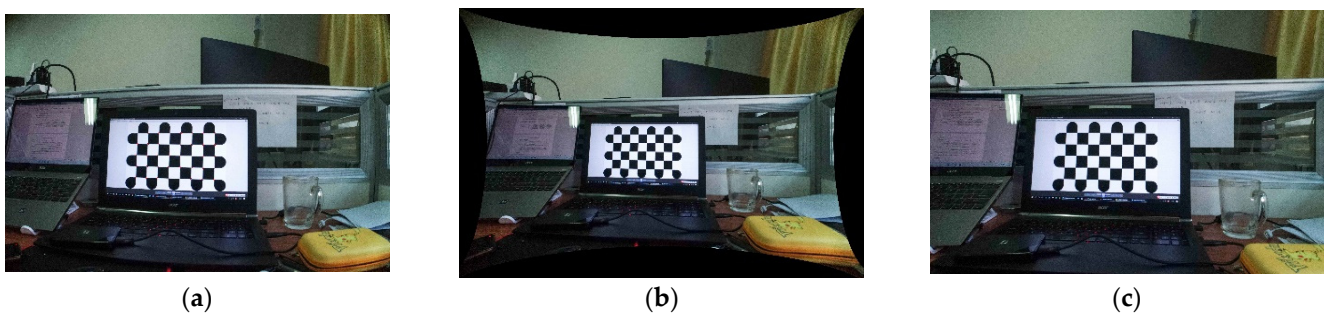

| (**a**) | (**b**) | (**c**) |

Figure 2. Distortion correction process, showing the (**a**) distorted image, (**b**) image after distortion correction, and (**c**) cut corrected image.

2.3. Cooperative Transform Shifting Parallax Method

The cooperative transform shifting parallax method was the core algorithm of the monocular visual digital photography technique used in this study [34,35]. It requires the photographic optical axis to be perpendicular to the reference plane. Moreover, the displacement of the deformation monitoring point was transformed into the real displacement of the deformation point, which was calculated according to the mathematical relationship between the photographic scales of the reference plane and the object surface (object plane) (Figure 3). The detailed deduction process is as follows:

Table 1. Internal camera parameters and distortion coefficients of the Samsung Galaxy S9 rear camera.

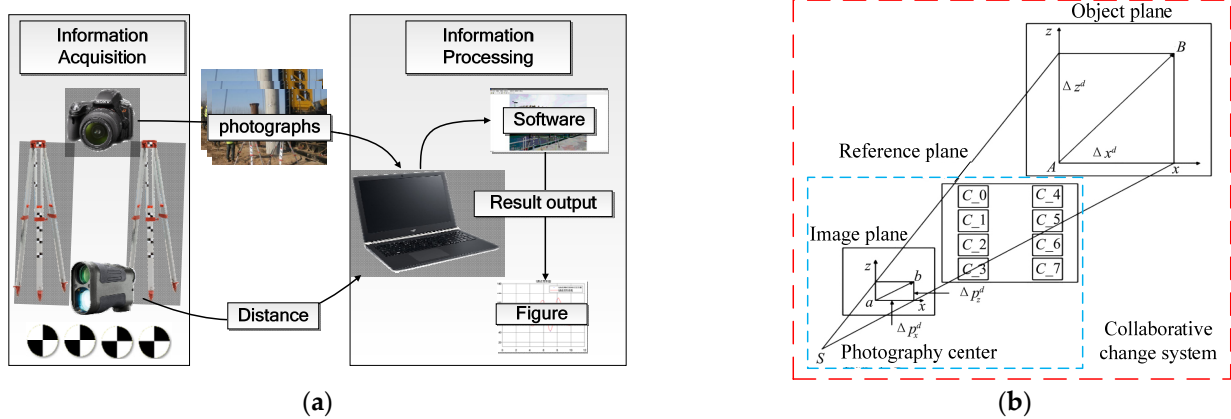| Calibration Method		PDMS	MATLAB
Camera internal parameters	f_x	3095.729583	3115.151478
	f_y	3081.980675	3101.594706
	c_x	1979.634456	1990.049731
	c_y	1510.257453	1513.00499
Average re projection error	Mean error in Pixel	0.2256	0.3800
Deformation parameters	k_1	0.286489	0.342840
	k_2	−1.464689	−1.956038
	p_1	−0.000442	0.000571
	p_2	−0.000537	−0.000147
	k_3	2.365860	3.615712

Figure 3. Cooperative transform shift parallax method, showing the (**a**) data acquisition and processing equipment and (**b**) principle of cooperative transform shift parallax method.

In Equation (3), Δx^{de} and Δz^{de} of the deformation point on images on the object plane can be expressed as follows:

$$\left.\begin{array}{l} \Delta x^{de} = \frac{SA}{Sa}\Delta p_x^{de} = m \times \Delta p_x^{de} \\ \Delta z^{de} = \frac{SA}{Sa}\Delta p_z^{de} = m \times \Delta p_z^{de} \end{array}\right\} \tag{3}$$

where m is the photographic scale of the reference plane. Δx^{de} and Δz^{de} are the horizontal and vertical displacements of the deformation points on the object plane, respectively. Δp_x^{de} and Δp_z^{de} are the horizontal and vertical parallax errors of the corresponding deformation points on images, respectively. Notably, Δp_x^{de} and Δp_z^{de} contain system errors at this time.

Δp_x^{de} and Δp_z^{de} can be expressed through Equation (4):

$$\left.\begin{array}{l} \Delta p_x^{de} = (x_2^{de} - x_1^{de}) - (dx_2^{de} - dx_1^{de}) \\ \Delta p_z^{de} = (z_2^{de} - z_1^{de}) - (dz_2^{de} - dz_1^{de}) \end{array}\right\} \tag{4}$$

where points $a(x_1^{de}, z_1^{de})$ and $b(x_2^{de}, z_2^{de})$ are the homonymy points on the zero image and subsequent images, respectively. Meanwhile, (dx_1^{de}, dz_1^{de}) and (dx_2^{de}, dz_2^{de}) are system errors of the homonymy deformation points on the zero image and subsequent image, respectively.

3. Dynamic Monitoring Test of the Standard Penetration of Large-Diameter Tubular Piles and the Relevant Construction Effect

In this paper, a case study was carried out on the renovation and expansion project along the section of the Beijing-Taipei High-Speed Rail Corridor from Dezhou (Shandong-Hebei Border) to Qihe. This region covers the alluvial plain of the Yellow River. The field test was performed in Pingyuan County, Dezhou City. The route is shown in Figure 4.
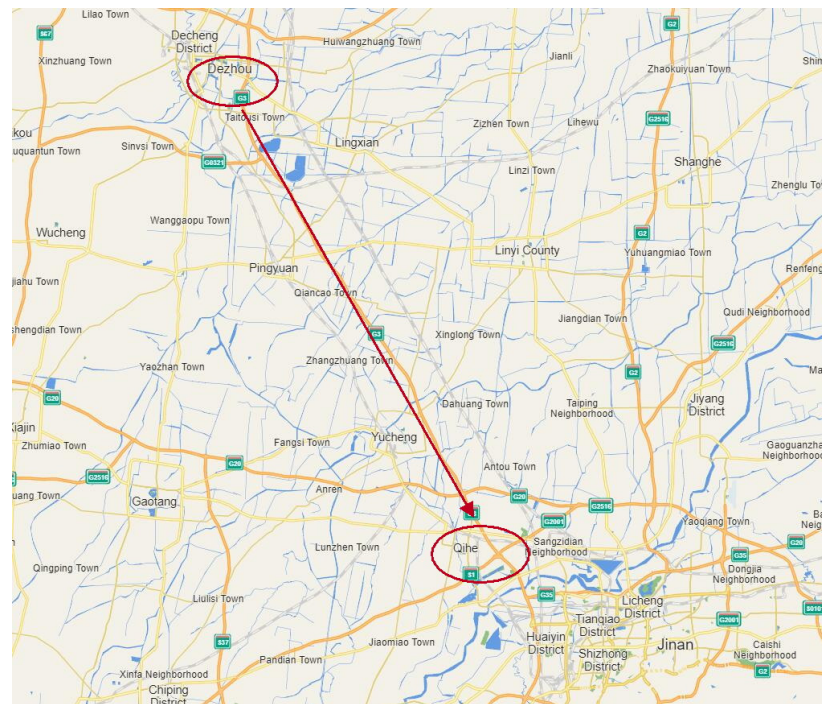
Figure 4. Geological location of the project.

Through field geotechnical explorations, the strata in the study area were found to be plain fill, plain fill, silt, silty clay, aleurite, silt, aleurite, fine sand, and silt, respectively (Table 2). Among them, the seventh layer of fine sand was relatively thick, and it was one of the choices for use as the bearing stratum at the pile end.

Table 2. Thickness and soil properties of different strata in the test site.

Geologic Age	Strata No.	Bottom Elevation (m)	Bottom Depth (m)	Thickness of Strata (m)	Description of Strata
Q4 al+pl	1	15.5	0.5	0.5	Plain fill: isabelline, loose, slightly humid, silt as the major component, with few plant roots.
Q4 al+pl	2	8.9	7.1	6.6	Silt: isabelline, slightly compact, slightly humid, uniform ingredients, high sand content.
Q4 al+pl	3	−1.2	17.2	10.1	Silty clay: yellow, 14.1–14.5 M. cinereus, plastic, locally thin silt strata, occasional iron and manganese oxides, moderate dry strength, moderate tenacity, smooth cutting surface.
Q4 al+pl	4	−3.2	19.2	2	Aleurite: isabelline, moderately compact, saturated, quartz and feldspar as major components, relatively pure arenaceous, good sorting performance, poor grading.
Q4 al+pl	5	−7.6	23.6	4.4	Silt: isabelline, compact, humid, thin layer with small clay soil content, moderate dry strength, poor tenacity.
Q3 al+pl	6	−10.1	26.1	2.5	Aleurite: isabelline, compact, saturated, quartz and feldspar as major components, relatively pure arenaceous, good sorting performances, poor grading.
Q3 al+pl	7	−26.1	42.1	16	Fine sand: isabelline, compact, saturated, quartz and feldspar as major components, relatively pure arenaceous, good sorting, poor grading.
Q3 al+pl	8	−34	50	7.9	Silt: brown, compact, humid, thin layer with small clay soil content, looks like multi-layer steamed bread, stinking smell, moderate dry strength, poor tenacity.

In this study, dynamic monitoring tests on the standard penetration of large-diameter tubular piles and monitoring tests on the construction effect were carried out at the con-

struction site and in an indoor environment. The experimental schemes and processes are as follows:

3.1. Dynamic Monitoring Test of Standard Penetration of Large-Diameter Tubular Piles

The designed length, pile diameter, and wall thickness of tubular piles for site operation were 47 m, 800 mm, and 60 mm, respectively. A rectangular arrangement was adopted for the piles (Figure 5a,b).
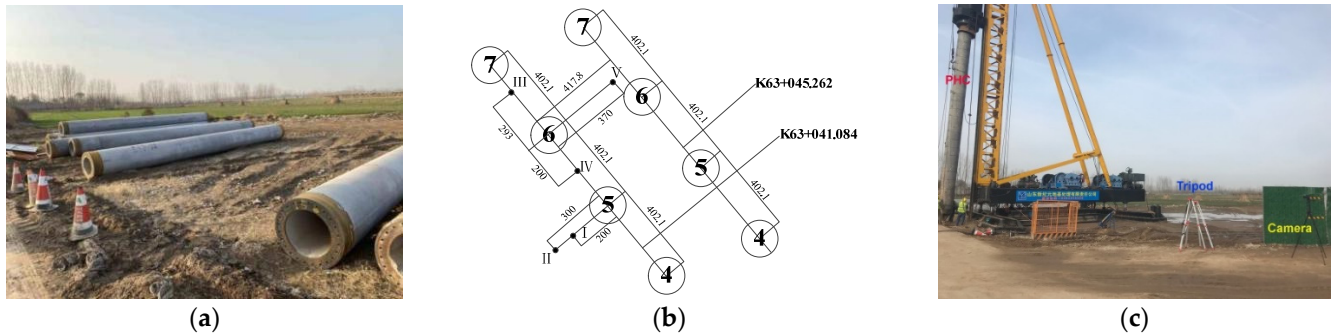

Figure 5. Field diagram of large diameter pipe pile penetration monitoring experiment, showing the (**a**) large diameter pipe pile, (**b**) rectangular pile arrangement, and (**c**) monitoring diagram.

Figure 5c shows that the control points and monitoring sites were set reasonably according to the requirements of the time-baseline parallax method. The digital camera and tripod were installed at appropriate positions in the stable zone, which was some distance away from the large-diameter tubular pile, to keep the camera stable throughout the test procedure. The tubular piles were about 15 m from the digital camera and about 2.5 m from the tripod. The experimental steps were as follows:

① Before the penetration of the tubular piles, several high-quality images were taken, and the optimal one was chosen as the initial image for comparison with subsequent images.

② During the penetration of tubular piles, an image was taken every 2 s to obtain the spatial position of the tubular pile at the given moment.

③ Finally, the abovementioned process was repeated for each test until all tubular piles were penetrated successfully. Further, image data were processed; the monitoring test sites are shown in Figure 6.

3.2. Field Tests on the Construction Effect of Large-Diameter Tubular Piles

The pile layout is shown in Figure 5b. Pile #6 has been fished, and it was about 1 m away from the earth's surface. To investigate the influences of Pile #4 and Pile #5 on Pile #6, the author developed a monitoring steel bar (Figure 7c) and welded it onto the surface of Pile #6 to measure its spatial displacement. Five reflector plates were pasted onto the self-made steel frame as monitoring sites. The monitoring equipment and monitoring sites are shown in Figure 7.

The layouts of the digital cameras and the monitoring process were comparable to the dynamic monitoring test of the standard penetration of large-diameter tubular piles. Tripods and digital cameras were set at 13 m and 15 m in front of the monitoring steel bar. Further, total-station instruments were installed freely near the digital cameras. Before the construction of Pile #4, the initial image and initial spatial coordinates of the self-made steel bar were acquired by the digital cameras and total-station instruments, respectively. The images and spatial coordinates of the self-made steel bar were acquired regularly throughout construction. These steps were repeated in the construction of Pile #5.
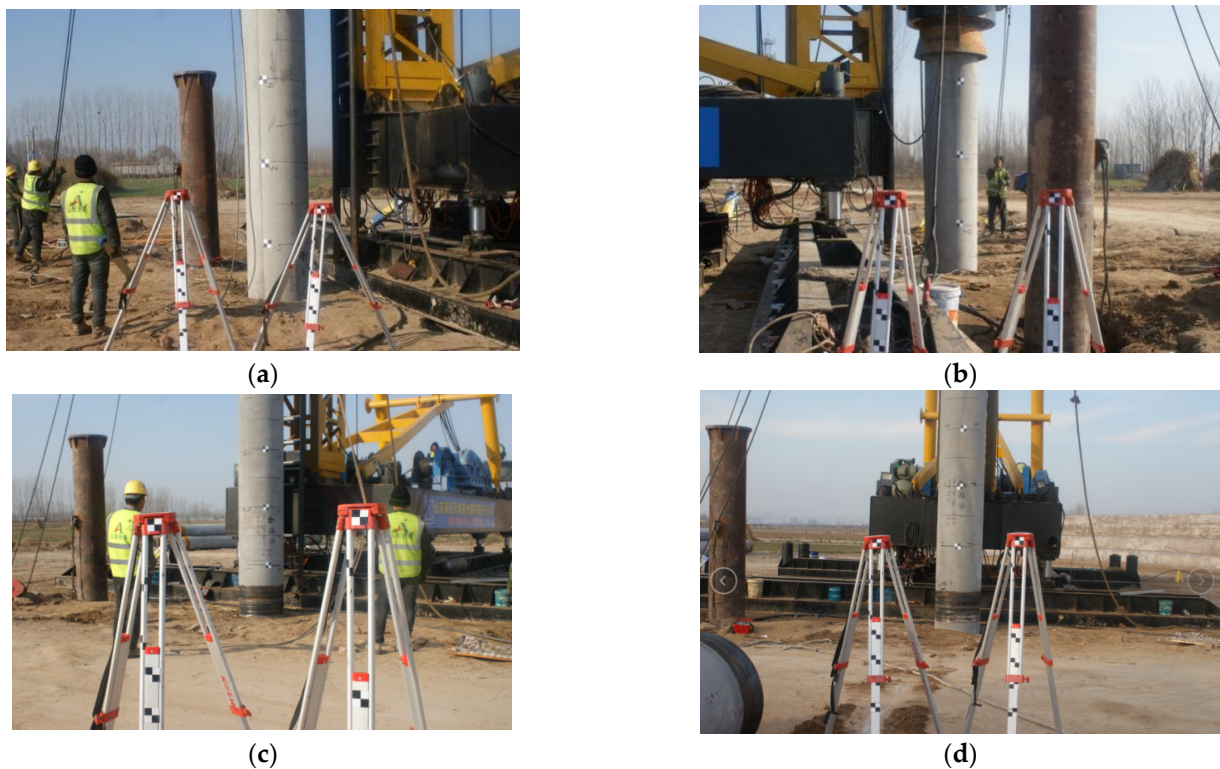
Figure 6. Large diameter Pipe Pile Penetration Monitoring Experiment Site, displaying the (**a**) test of the first pipe pile at No. 6 pile site, (**b**) test of the second pipe pile at No. 6 pile site, (**c**) test of the third pipe pile at No. 6 pile site, and (**d**) test of the fourth pipe pile at No. 6 pile site.
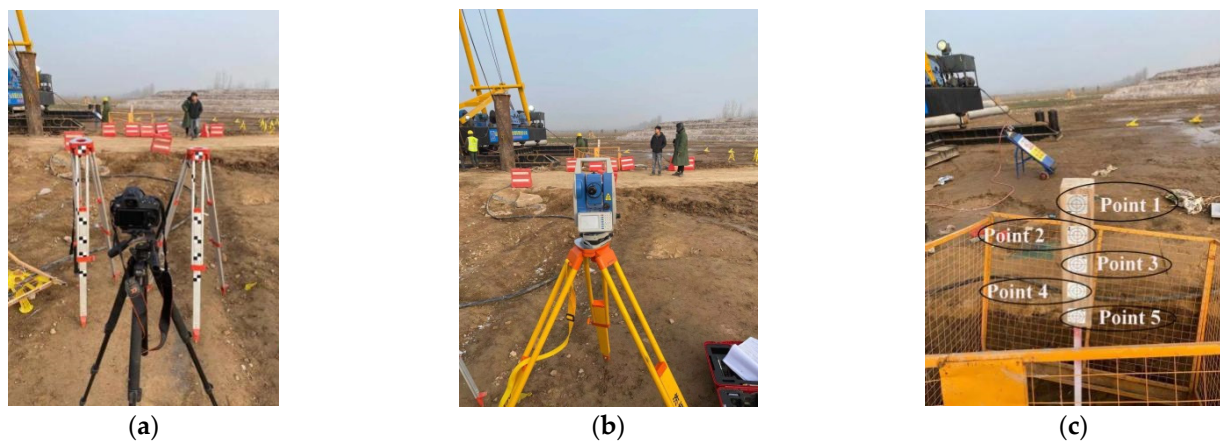

Figure 7. Site schematic diagram of large diameter pipe pile construction effect experiment, showing the (**a**) digital camera, (**b**) total station, and (**c**) self-made monitoring steel pole.

3.3. Indoor Tests on the Construction Effect of Large-Diameter Tubular Piles

The self-designed device was applied to simulate squeezed soils, the soil plug phenomenon, and the bearing capacity of open-ended tubular piles during settlement. The test model groove was a 100 cm (length) × 40 cm (width) × 80 cm (height) rectangular tempered glass box with an open upper end; the tempered glass pieces were connected by binding. The layered pavement was applied as sample loading in the experiment, and layering was visualised using dyeing sands. The displacement changes in soil plugs at different positions in the tubular pile could be seen clearly during penetration. The loading support in the test and the physical image are shown in Figure 8.
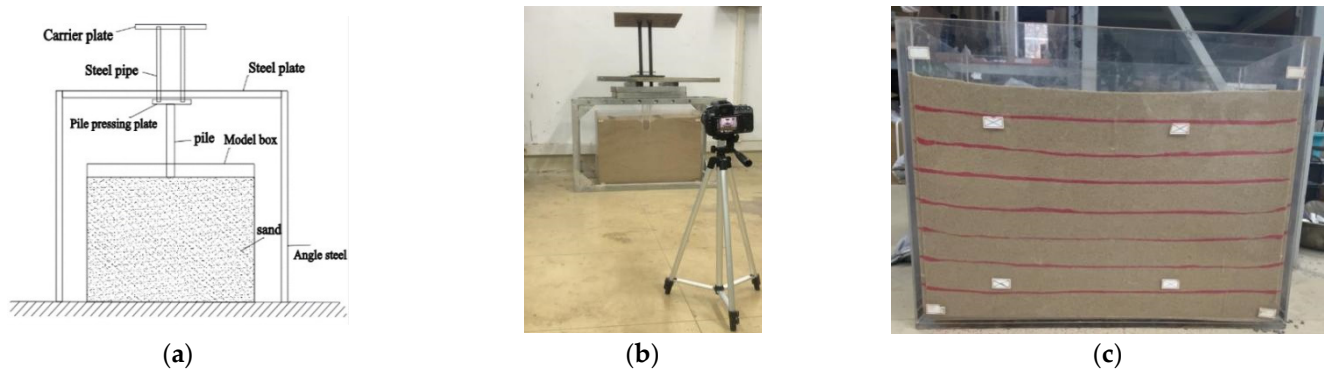
Figure 8. Experiment and schematic diagram, showing the (**a**) schematic diagram of model design, (**b**) laboratory test site, and (**c**) model box with stained sand.

The test steps were similar to those of the dynamic monitoring test of the standard penetration of large-diameter tubular piles. The digital camera is 1.5 m away from the model device, the photographic optical axis is perpendicular to the monitoring surface of the model device, and control points are laid on the monitoring surface of the model box (white cubes in Figure 8c). The lines between the control points constitute the regions shown in the study. The experimental steps were as follows:

① Before a pipe pile penetration test, several high-quality images were taken, and the optimal one was chosen as the initial image for comparison with subsequent images.

② After the pipe pile penetration test, one image was taken to obtain the final spatial position of the tubular pile.

③ Finally, the above-mentioned process was repeated for each test, image data were processed.

4. Data Processing and Analysis

4.1. Standard Penetration Data Analysis of Large-Diameter Tubular Piles

In the test, the pixel displacements of the reference points were supposed to be zero in theory. However, their pixel displacements were not zero in the cooperative transform shifting parallax method. As such, these values were deemed as the measurement accuracy of pipe pile penetration test. Due to the large amount of data, the authors selected 12 tests of pipe pile 1–2 penetration test for data processing. The measurement accuracy is shown in Table 3. In Table 3, 1-Point 0, 1-Point 1, and 1-Point 2 represent the control point 0, 1, and 2 in pipe pile #1 penetration test. 2-Point 0, 2-Point 1, and 2-Point 2 represent the control point 0, 1, and 2 in pipe pile #2 penetration test. MSE is mean square error, its maximum is 0.84 mm, and its minimum is 0.14 mm.

Table 3. Measurement Accuracy of Camera/mm.

Blow Counts	Pile 1 Blow Test			Pile 2 Blow Test		
	1-Point 0	1-Point 1	1-Point 2	2-Point 0	2-Point 1	2-Point 2
1	0	0.73	0.73	0.99	0	0
2	0	0	0.73	0.99	0	0
3	0	0	0.73	0.49	0	0
4	−0.73	0	0.73	0.99	0	0
5	−0.73	0.73	0	0.49	−0.49	0
6	0	0	0.73	0.49	0	0
7	−0.73	0	0	0.99	0	−0.49
8	−0.73	0.73	0	0.99	0	0
9	0	0	0.73	0.99	0	0
10	0	0	0.73	0.49	0	0
11	0	0	0.73	0.99	−0.49	0
12	0	0	0.73	0.49	0	0
MSE	0.42	0.37	0.63	0.82	0.20	0.14

The penetration data of tubular piles at different time points were acquired through image processing (Table 4). Figure 9a,b show that a Logistic functional relationship exists between the penetration and blow counts. The penetration rate of Pile #1 was relatively large, and it penetrated the strata completely after 12 blow counts. This indicates that the soil structure at 0–10 m below the surface was relatively loose, agreeing with the observations regarding actual strata.

Table 4. Monitoring data of pipe pile penetration at No. 6 pile position.

Hit Times	Displacement/m	Hit Times	Displacement/m	Hit Times	Displacement/m
1	0.099	42	6.190	83	8.801
2	0.157	43	6.323	84	8.883
3	0.267	44	6.433	85	8.921
4	0.314	45	6.430	86	8.922
5	0.388	46	6.605	87	8.960
6	0.460	47	6.626	88	8.997
7	0.596	48	6.885	89	9.046
8	0.605	49	6.948	90	9.084
9	0.704	50	6.977	91	9.124
10	0.832	51	7.100	92	9.220
11	0.883	52	7.159	93	9.257
12	0.940	53	7.190	94	9.287
13	1.310	54	7.317	95	9.327
14	1.505	55	7.372	96	9.364
15	1.622	56	7.398	97	9.403
16	1.786	57	7.488	98	9.408
17	1.937	58	7.551	99	9.507
18	1.993	59	7.604	100	9.523
19	2.364	60	7.692	101	9.548
20	2.595	61	7.737	102	9.605
21	2.780	62	7.786	103	9.593
22	2.978	63	7.851	104	9.671
23	3.073	64	7.900	105	9.663
24	3.519	65	7.962	106	9.705
25	3.790	66	8.016	107	9.782
26	3.986	67	8.027	108	9.819
27	4.113	68	8.081	109	9.868
28	4.149	69	8.135	110	9.911
29	4.658	70	8.244	111	9.931
30	4.655	71	8.301	112	9.978
31	4.763	72	8.308	113	10.007
32	4.877	73	8.353	114	10.051
33	4.997	74	8.409	115	10.079
34	5.045	75	8.442	116	10.118
35	5.143	76	8.466	117	10.186
36	5.187	77	8.552	118	10.191
37	5.455	78	8.631	⋮	⋮
38	5.617	79	8.672	⋮	⋮
39	5.736	80	8.708	151	11.507
40	5.833	81	8.781	152	11.541
41	5.914	82	8.791	153	11.535

Figure 9c,d show that a single exponential decay function relationship exists between penetration and blow counts. The penetration rate increased first and then decreased, and Pile #2 penetrated the strata completely after 153 blow counts. Pile #2 penetrated about 7.69 m after 60 blow counts. At this moment, it had passed through the loose silt and silty clay strata. Subsequently, it entered the stratum dominated by aleurite, leading the penetration rate to decrease due to the hard texture.

Since Pile #3 had the highest number of blow counts, several images existed for analysis. Hence, the penetration data of Pile #3 were divided into four stages to facilitate independent processing. In Figure 10a–d, we can see the spatial evolution patterns of the underground part and the above-ground part of the pipe pile in four monitoring stages. It can be seen from Figure 10e,f that the penetration rates of Pile #3 show a trend of single exponential decay functions. However, the penetration rate of Pile #3 was significantly

lower than those of Pile #1 and Pile #2. Pile #3 was penetrated completely after 1200 blow counts. Currently, the bottom of Pile #3 was in the aleurite. Moreover, the strata pressure increased with increases in depth, making soils harder and harder. Consequently, the penetration rate of Pile #3 was relatively low.
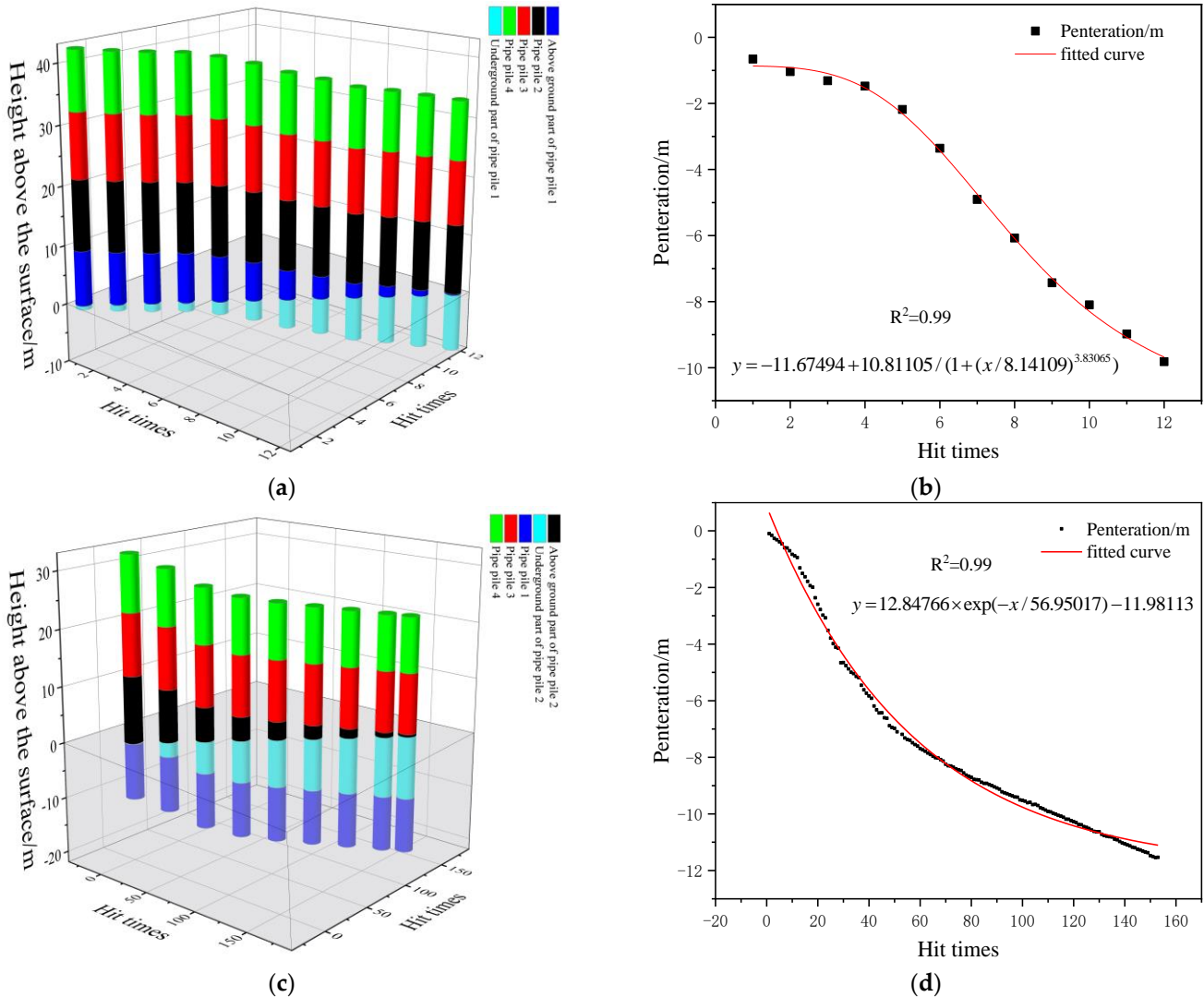

Figure 9. Schematic diagram of penetration change in first and second pipe piles at pile position 6, displaying the (**a**) spatial diagram of penetration evolution law of pipe pile 1, (**b**) fitting analysis of penetration evolution law of pipe pile 1, (**c**) spatial diagram of penetration evolution law of pipe pile 2, and (**d**) fitting analysis of penetration evolution law of pipe pile 2.

Similarly, the data of Pile #4 were divided into three stages for independent processing and fitting. In Figure 11a–c, we can see the spatial evolution patterns of the underground part and the above-ground part of the pipe pile in three monitoring stages. It can be seen from Figure 11d,e that the penetration rates of Pile #4 show a trend of the piecewise linear function. Its slope decreases first and then increases suddenly.

Based on the abovementioned analysis, an obvious turning point exists in the penetration rate of Pile #4 around the 500th blow count. This demonstrated that Pile #4 penetrated through the relatively hard aleurite into the relatively soft silt and further approached the bearing stratum.
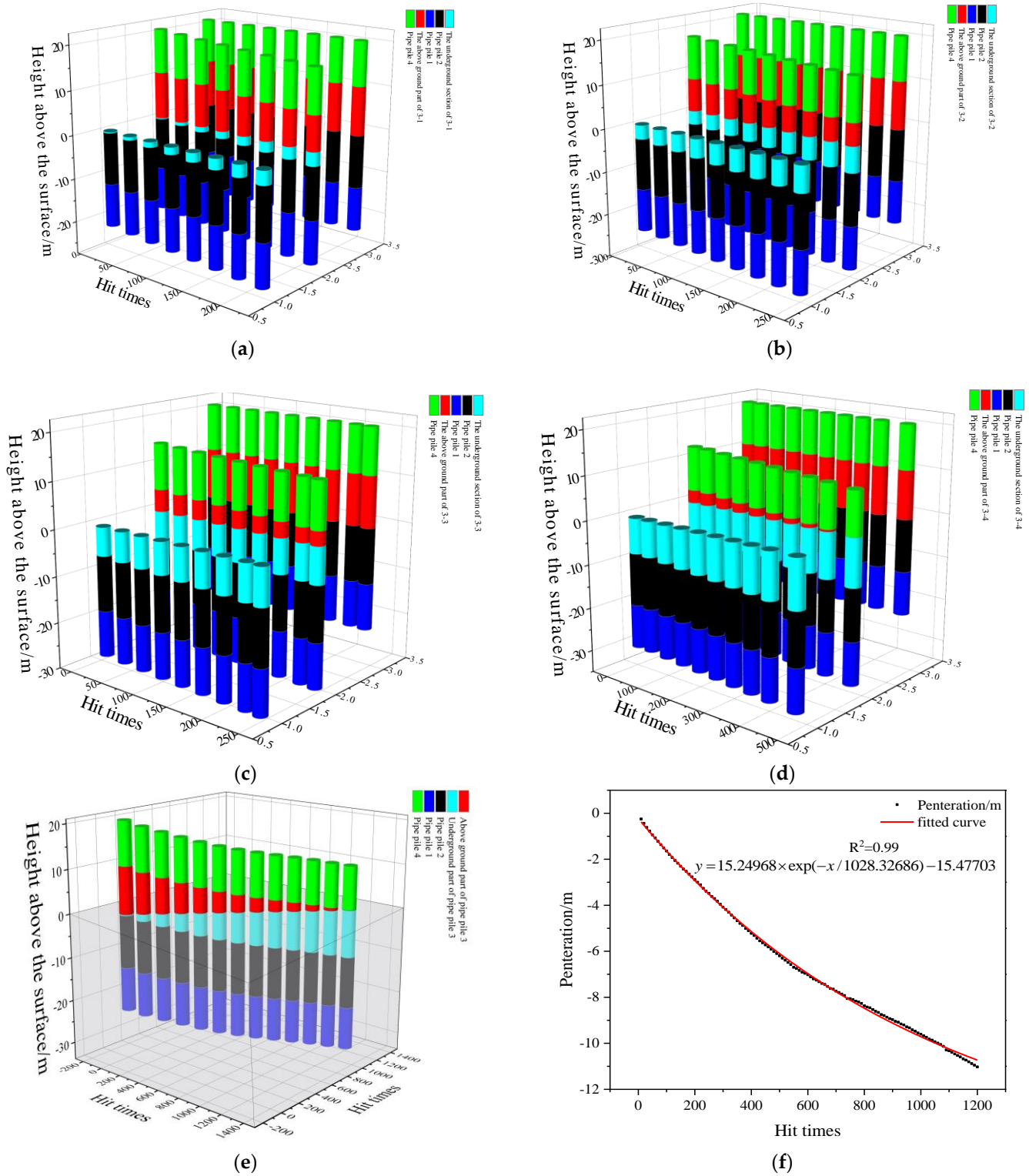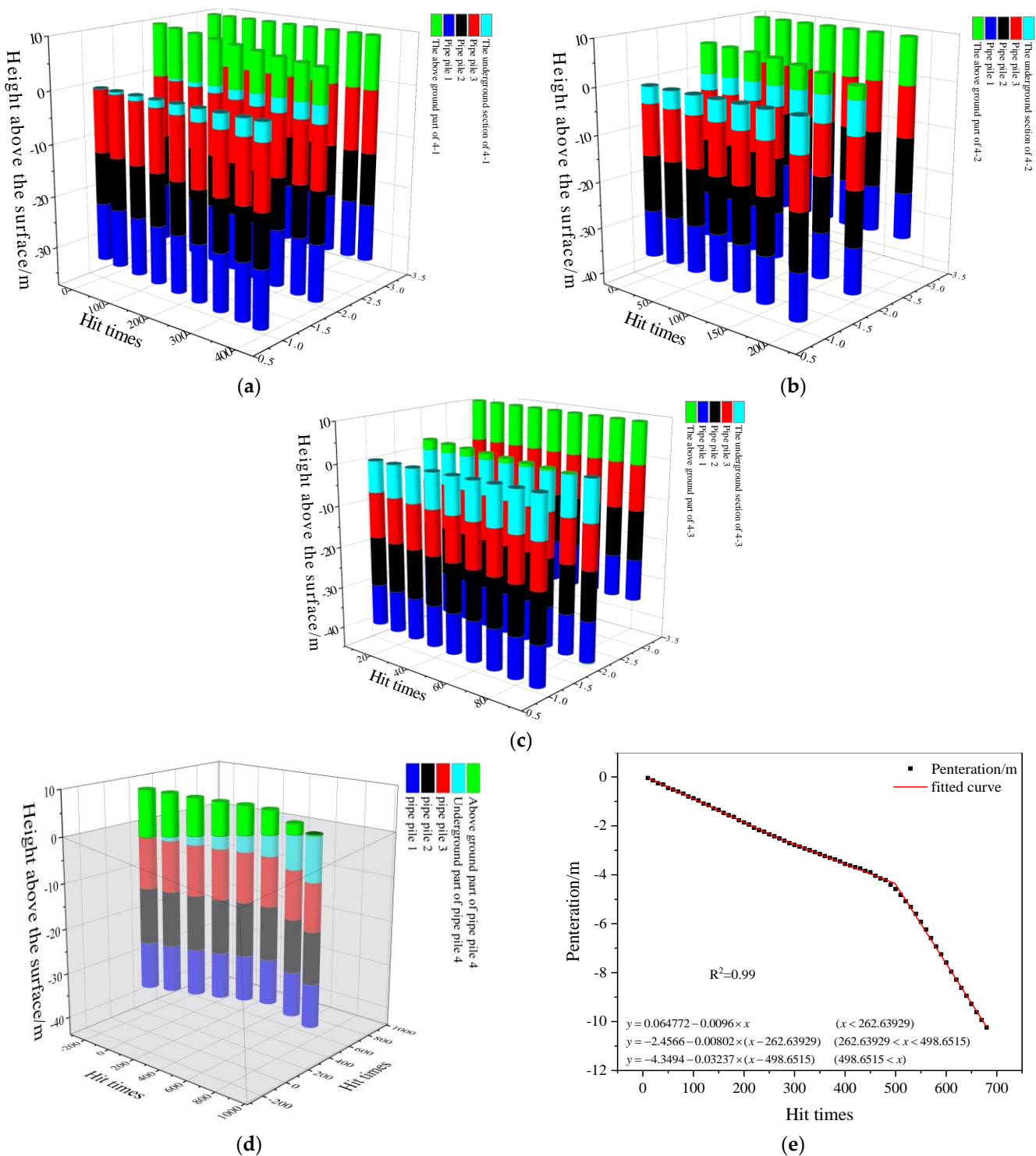
Figure 10. Schematic diagram of penetration evolution of pipe pile 3 at pile position 6, showing the (**a**) schematic diagram of pipe pile penetrated the strata in first monitoring stage, (**b**) schematic diagram of pipe pile penetrated the strata in second monitoring stage, (**c**) schematic diagram of pipe pile penetrated the strata in third monitoring stage, (**d**) schematic diagram of pipe pile penetrated the strata in fourth monitoring stage, (**e**) spatial diagram of penetration evolution law, and (**f**) fitting analysis of penetration evolution law.

Figure 11. Diagram of penetration evolution of the 4th pipe pile at pile 6, showing the (**a**) schematic diagram of pipe pile penetrated the strata in first monitoring stage, (**b**) schematic diagram of pipe pile penetrated the strata in second monitoring stage, (**c**) schematic diagram of pipe pile penetrated the strata in third monitoring stage, (**d**) spatial diagram of penetration evolution law, and (**e**) fitting analysis of penetration evolution law.

On this basis, the variation curves of the penetration of large-diameter tubular piles were plotted. In Figure 12a, the penetration and the corresponding blow counts evolve as a piecewise function, which is a logarithmic function in the early stage, a gently sloping

linear function in the middle stage, and a sharply sloping linear function in the late stage. According to the variations in the penetration and penetration rates at different stages, the geological conditions of tubular piles could be assessed intuitively concerning their locations. On this basis, the blow frequency and blow loads of the tubular piling machine could be adjusted promptly.
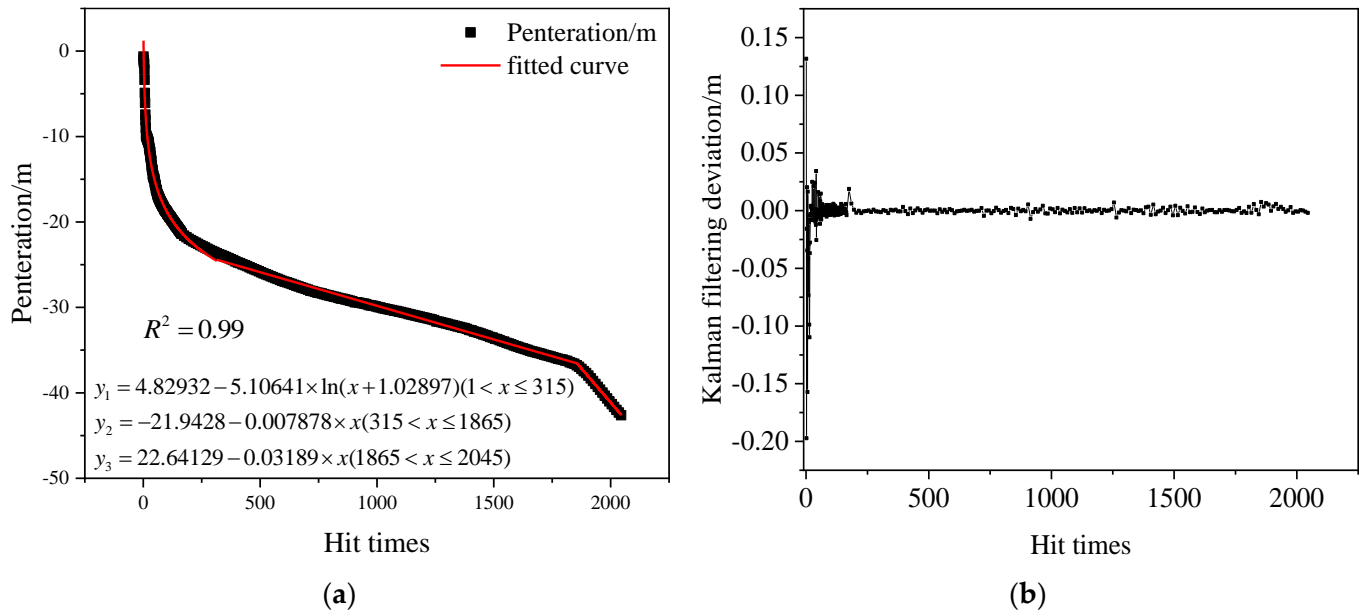

(a)

(b)

Figure 12. Diagram of penetration change in large diameter pipe pile at pile position 6, showing the (**a**) fitting analysis of penetration evolution law at pile position 6, and (**b**) sketch of the penetration Kalman filter deviation.

Additionally, Figure 12b shows that monocular visual digital photography can meet the requirements concerning the standard penetration monitoring accuracy of large-diameter tubular piles. It can provide reliable basic data for the planning and design of deep foundations, facilitating the proposal of reasonable suggestions for unstable geological conditions. This can help improve the success rate of field construction significantly.

4.2. Field Monitoring Data Analysis of the Construction Effect of Large-Diameter Tubular Piles

The spatial displacements of observation points 1–5 during the construction of Position 5 and Position 4 were acquired through a combination of the data from the digital camera and station instrumentation. To express the positional evolution state of Position 6 accurately and clearly, the mean measuring results of observation points 1–5 were calculated, and the corresponding diagram was plotted (Table 5 and Figure 13).

Table 5. Movement value of the monitored pile (A-6).

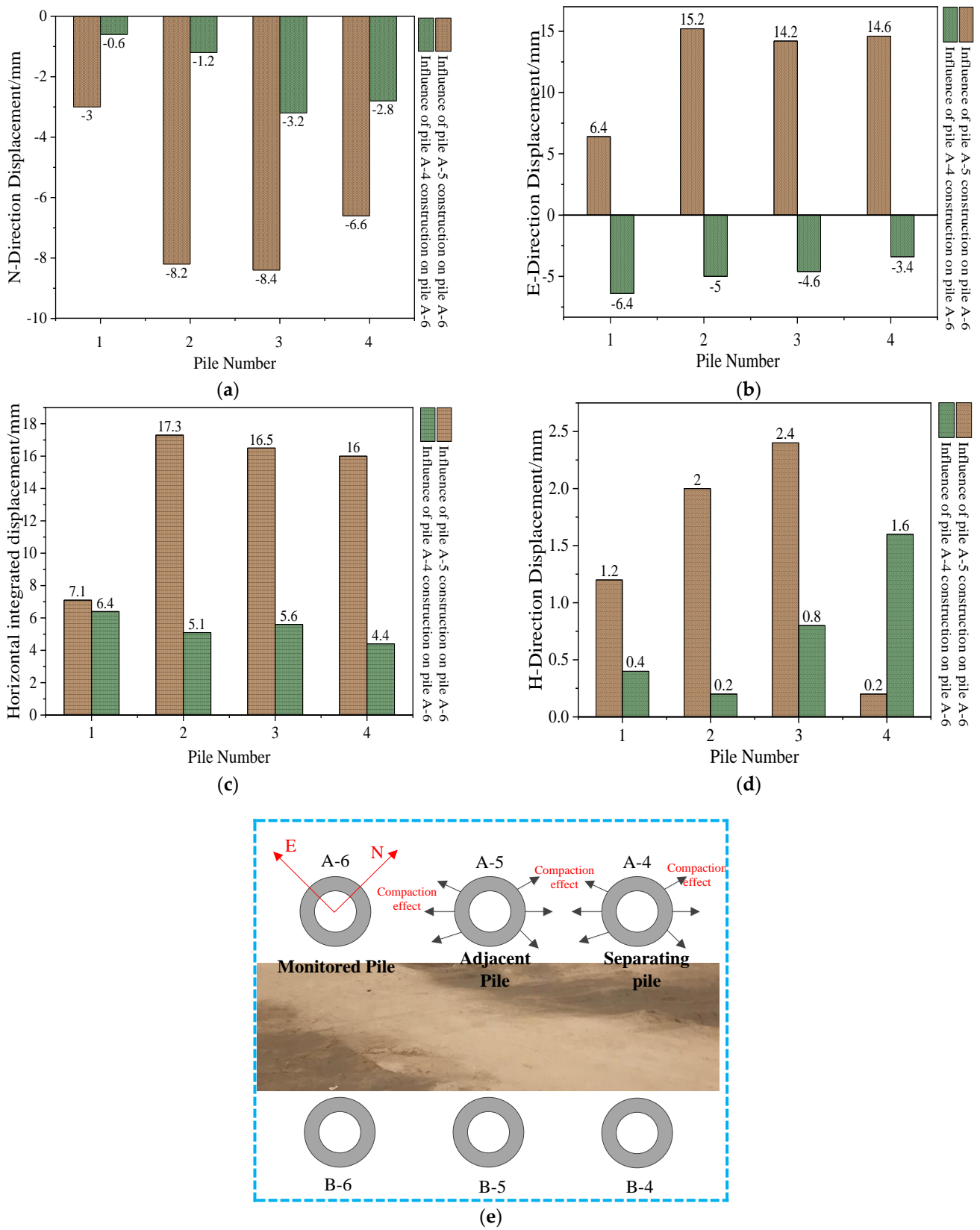| Pipe Pile Number	Displacement in N Direction/mm		Displacement in E Direction/mm		Displacement in H Direction/mm	
	Construction of A-5	Construction of A-4	Construction of A-5	Construction of A-4	Construction of A-5	Construction of A-4
1	−3.0	−0.6	6.4	−6.4	1.2	0.4
2	−8.2	−1.2	15.2	−5.0	2.0	0.2
3	−8.4	−3.2	14.2	−4.6	2.4	0.8
4	−6.6	−2.8	14.6	−3.4	0.2	1.6

Figure 13. Representation of space displacement and compaction effect, showing the (**a**) schematic diagram of N-direction displacement, (**b**) schematic diagram of E-direction displacement, (**c**) schematic diagram of horizontal displacement, (**d**) schematic diagram of H-direction displacement, and (**e**) relationship between compaction effect and space displacement.

Figure 13a,e show that, during the construction of Piles #1, #2, #3, and #4 at Position 5, Position 6 deviated by 3 mm, 8.2 mm, 8.4 mm, and 6.6 mm along the S direction, respectively. During the construction of Piles #1, #2, #3, and #4 at Position 4, Position 6 deviated by 0.6 mm, 1.2 mm, 3.2 mm, and 2.8 mm along the S direction, respectively. According to the measurement data, Position 6's squeezing effect strengthened first and then weakened with increases in the penetration of tubular piles.

In Figure 13b,e, Position 6 deviated by 6.4 mm, 15.2 mm, 14.2 mm, and 14.6 mm along the E direction during the construction of Piles #1, #2, #3, and #4 at Position 5, respectively. During the construction of Piles #1, #2, #3, and #4 at Position 4, Position 6 deviated by 6.4 mm, 5 mm, 4.6 mm, and 3.4 mm along the E direction, respectively. According to measurement data, Position 6 was squeezed away and rebounded along the E direction. This phenomenon indicates that the squeezing effect strengthened first and then weakened with increases in the penetration of tubular piles.

Figure 13a–e show that the squeezing effect peaked when the penetration depth of the tubular piles was about 20 m during the construction at adjacent positions, which could make surrounding tubular piles deviate from the initial position by nearly 2 cm. During the pile-jumping construction, the squeezing effect was relatively weak. The maximum squeezing effect was observed when the penetration depth of tubular piles was about 10 m, which could make the tubular piles deviate from the initial position by about 0.5 cm. The experimental results in this study further verified the reliability of pile-jumping construction technology and provided reference data for its optimisation.

Figure 13d,e showed that a slight uplift was developed during the construction of adjacent piles and pile-jumping construction. This was the collaborative consequence of increasing the short installation and side friction resistance under the squeezing effect.

4.3. Plugging Effect Analysis of Large-Diameter Tubular Piles

An obvious plugging effect was observed in the indoor tests on large-diameter tubular piles when they penetrated the strata. Displacement variations in three stages of the plugging effect are shown in Figure 6. Figure 14a–c show that, in the early piling stage, foundation soils suffered shear failure due to the influence of the pile wall. Meanwhile, the soil mass below the pile wall close to the pile end developed shear displacement. However, the soil mass in the piles did not move downward significantly as the pile penetrated further.

Figure 14d–f show that the soil plug height and the frictional force between the soil plug and pile wall increased with increases in the penetration depth of tubular piles. Under these circumstances, the soil plug moved downward continuously due to frictional resistance. Accordingly, the altitude difference between the top surface of the soil plug and the original sand surface increased. Since the shear deformation near the pile wall was larger than that of sand particles in the middle of the soil plug, the dyeing sand layer was 'convex'. Further, and the soil plugs in piles produced a 'convex' arch due to frictional resistance.

Figure 14g,h show that, as the piles pressed in continuously, the soil plug was compacted gradually due to the combined action of downward frictional resistance with the pile wall and the counterforce of the soil mass at the pile end. The dyeing sand layer developed a ball cap-like 'concave' arch. The soil plug in the pile developed an extremely large frictional force, stopping the further inrush of the soil mass into the pile like a 'bottle plug'. The length of the soil plug did not increase any more after this, reflecting a significant plugging effect. Consequently, the bearing characteristics of open-ended piles were the same as those of closed-ended ones.
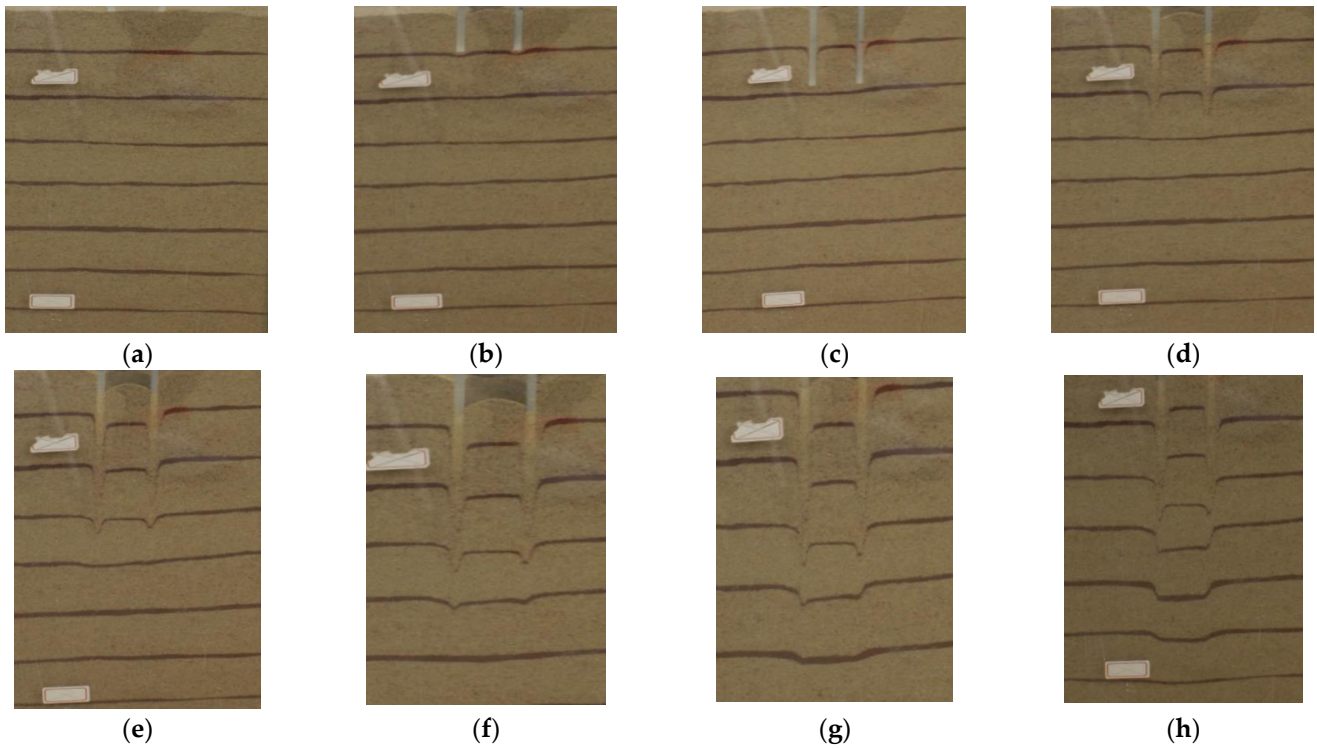
Figure 14. Soil plug phenomenon of pipe pile (**a**) before pressing piles, (**b**) at the pressed depth of 50 mm, (**c**) at the pressed depth of 100 mm, (**d**) at the pressed depth of 150 mm, (**e**) at the pressed depth of 200 mm, (**f**) at the pressed depth of 250 mm, (**g**) at the pressed depth of 300 mm, and (**h**) at the pressed depth of 350 mm.

Additionally, a displacement contour map of the foundation soil was also drawn when the model piles penetrated the strata. The sphere of influence and size of the plugging effect were analysed quantitatively.

Figure 15 shows that the horizontal and longitudinal spheres of influence expanded gradually as the piles settled. However, the vertical influences were significantly more obvious than the horizontal influences. The contour lines in the vertical and horizontal spheres of influence were rectangular. Model piles may have developed a horizontal squeezing effect when the plugging effect began to form. The horizontal sphere of influence of the squeezing effect also expanded severalfold.
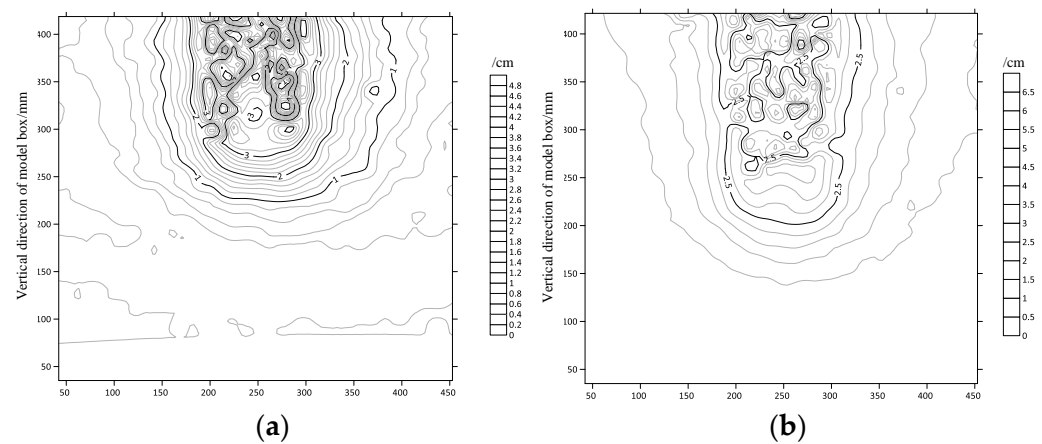

Figure 15. Soil body displacement contour diagram for different penetration of piles at the (**a**) pile penetration of 100 mm, and (**b**) pile penetration of 150 mm.

4.4. Squeezing Effect Analysis of Large-Diameter Tubular Piles

In the data processing, the images are first loaded in the software, and then the control point file is established. Last, the authors run the image analysis program Geodog and post processor Post Viewer to carry out pixel and displacement solution.

The cloud chart of soil mass displacement at different penetration depths was obtained from data processing. It can be seen from Figure 16 that, in the early penetration stages, the piles arrived at a superficial soil mass. Even though soil mass, within a certain level at the pile bottom, mainly moved downward laterally, the surrounding soil mass was mainly squeezed out laterally. With increases in the penetration depth, the rising trend of the deep soil mass was weakened, and the surrounding soil mass developed vertical displacement and deformation relative to the pile body. Radial squeezing played a dominant role in most regions. Moreover, a spherical disturbed area would be formed at the bottom of the pile. The scope of this area was related to the initial state of the soil mass, such as relative compaction (Figure 18).
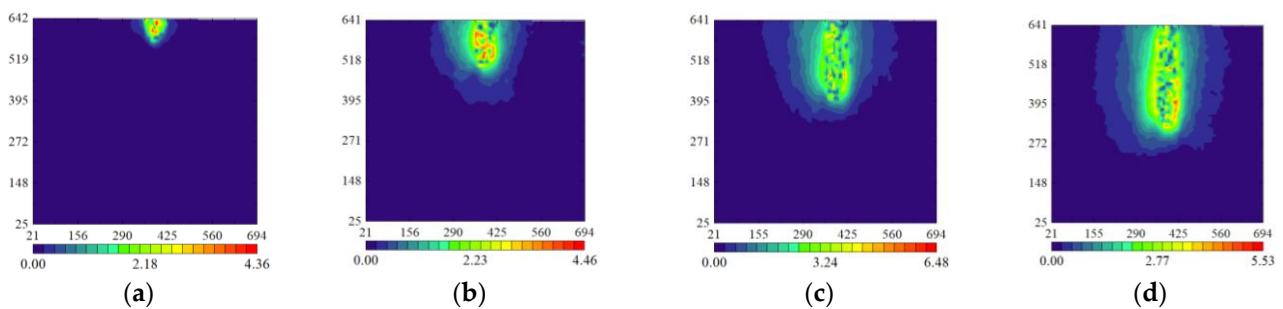

Figure 16. Cloud diagram of pipe pile penetration displacement when (**a**) penetrated into 1/4 pile length, (**b**) penetrated into 2/4 pile length, (**c**) penetrated into 3/4 pile length, and (**d**) penetrated into 4/4 pile lengths.

To study the spatial variation laws of the displacement deformation of the surrounding piles of the soil mass, as well as the effective sphere of influence, vertical observation belts were set at one, three, five, seven, and nine times the pile diameter away from the pile after it was penetrated completely. Moreover, horizontal monitoring belts were set at 0 cm, 8 cm, 16 cm, 24 cm, 32 cm, 40 cm, 48 cm, and 56 cm away from the soil mass surface. The variation curves of the vertical soil displacement at different distances away from the pile and soil displacement at different depths were also drawn (Figure 17).
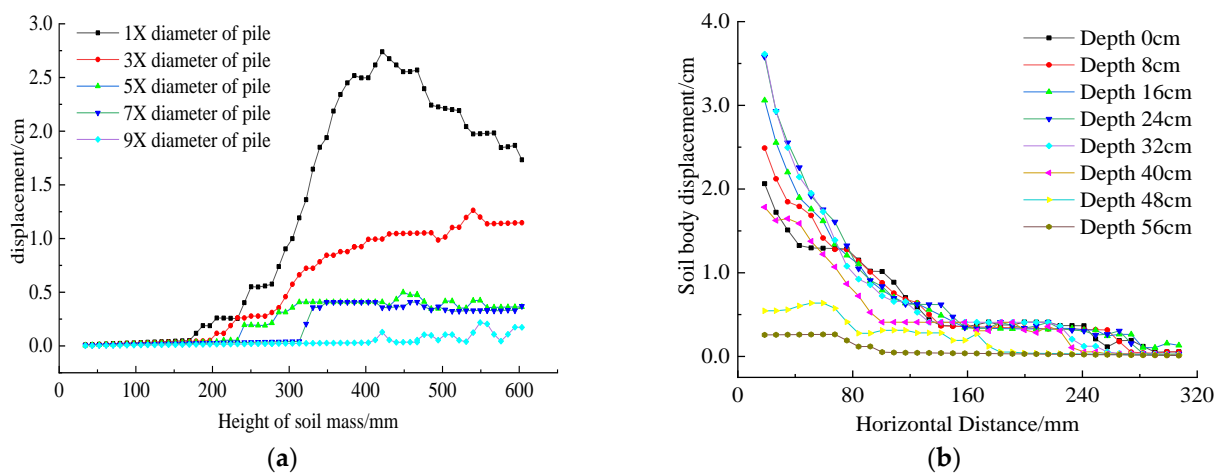

Figure 17. Influencing factors of soil displacement around piles and response law curve for the (**a**) curve of relationship between soil body displacement and the depth along pipe pile and (**b**) relationship curve between soil body displacement and distance from pipe pile.

Figure 17a shows that the vertical soil displacement increased first and then decreased with increases in the distance from measuring points to the central axis of the pile body. The soil displacement approached 0 at the position, which was nine times the pile diameter away. It could be viewed as the boundary of the radial squeezing zone. Figure 17b reflected that, in the penetration depth range of piles, the horizontal displacement of the soil mass followed an exponential function. The radial displacement slowly approached 0 when the penetration depth was 1.5 times the pile length, forming a hemispherical expansion area [36–39]. The squeezing effect of the penetrated piles is shown in Figure 18.
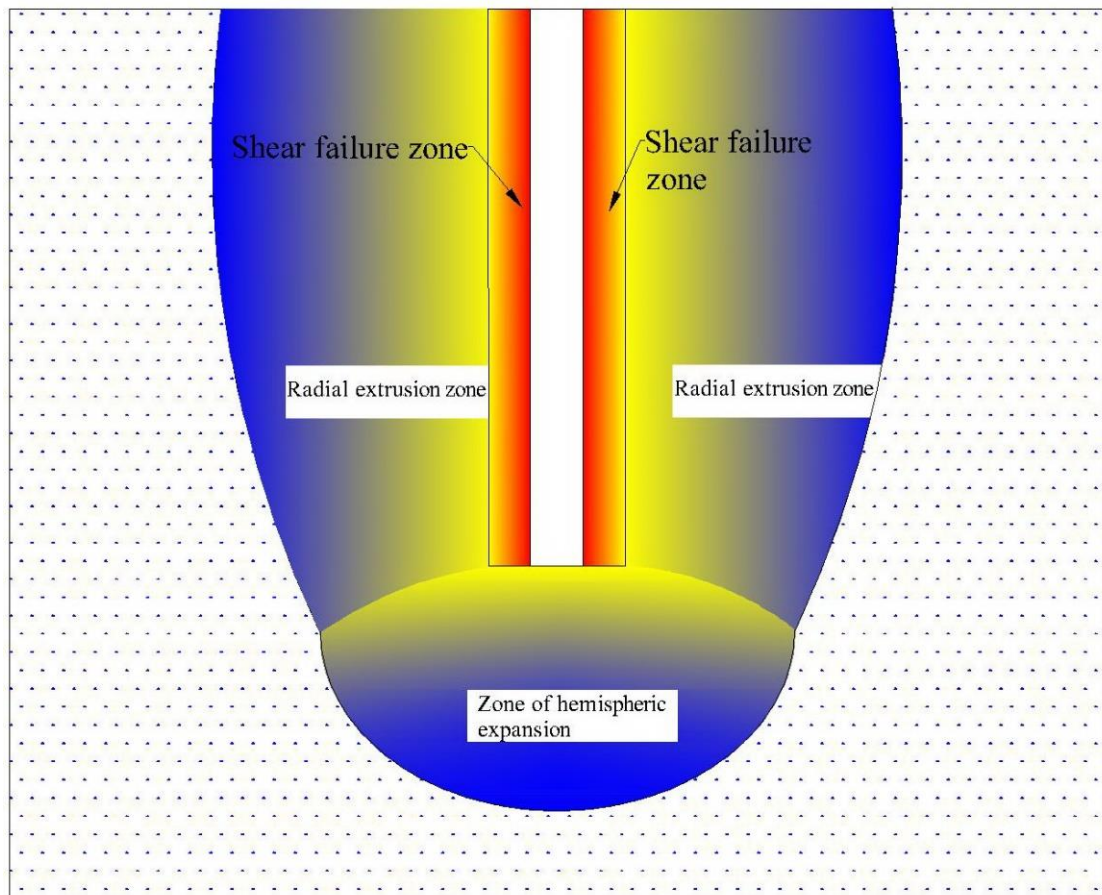

Figure 18. Affect region of a pile penetrating the strata.

5. Conclusions

Based on the highway construction project from Jinan to Gaoqing, the standard penetration of large-diameter tubular piles was monitored at a construction site based on monocular visual digital photography. Moreover, an indoor test model was developed per practical engineering conditions to study the construction effect of large-diameter tubular piles. Some major conclusions could be drawn.

(1) When large-diameter tubular piles penetrate from the loose stratum to aleurite and then to silt, the relationship between the penetration and time function (blow counts) evolves as a piecewise function. This, which is a logarithmic function in the early stage, a gently sloping linear function in the middle stage, and a sharply sloping linear function in the late stage. The penetration rates vary significantly under different strata conditions.

(2) According to the measurement data regarding pile deviation, the squeezing effect increases and then weakens during adjacent pile construction and pile-jumping construction. The maximum squeezing effect is observed as the adjacent pile is penetrated by about 20 m or the jumping pile is penetrated by about 10 m. The monitored pile is

influenced greatly by the construction of adjacent piles, similar to the results of the pile-jumping construction method.

(3) The plugging effect can be divided into three stages: the formation of a soil plug, increases in the frictional force between the soil plug and pile wall, and closure. In the first stage, it is manifested as a convex arch. In the second stage, the soil plug gradually changes from a convex arch to a concave arch. In the third stage, the soil plug is closed completely. Such engineering characteristics are similar to those of closed-ended piles.

(4) The horizontal and longitudinal spheres of influence of surrounding soil masses expand gradually with increases in the penetration depth of tubular piles. More specifically, vertical influences are significantly greater than horizontal influences. The contour lines the of vertical and horizontal spheres of influence form a rectangular distribution.

(5) When the plugging effect of a tube is closed, a horizontal squeezing effect of the surrounding piles of soil mass is developed. The horizontal sphere of influence expands, including the shear failure zone, radial compression zone, and hemispherical expansion zone. Among them, the radial compression zone is expanded to the point where it is nine times the pile diameter away from the pile axis, and the hemispherical expansion zone extends to the depth where it is 1.5 times the pile length.

In conclusion, digital photography technology is innovatively applied to the field monitoring process of large diameter pipe piles, which provides a cost-effective technical means to obtain the dynamic penetration value of large diameter pipe piles, and these data are of great significance to the field construction and optimization design of large diameter pipe piles. At the same time, digital photography technology can realize high-precision dynamic monitoring of the penetration value of large-diameter pipe piles in laboratory tests, which provides technical support for studying the dynamic evolution law of large-diameter pipe pile construction effect and optimizing construction parameters.

Author Contributions: Writing—review and editing, G.Z. and S.Z.; formal analysis, Z.L.; writing—original draft, W.X. and S.L.; investigation, Z.W. and Y.W. All authors have read and agreed to the published version of the manuscript.

Institutional Review Board Statement: Not applicable.

Informed Consent Statement: Not applicable.

Data Availability Statement: The data used to support the findings of this study are available from the corresponding author upon request (g_j_zhang@cumt.edu.cn).

Conflicts of Interest: The authors declare no conflict of interest.

References

1. Zhou, Y.; Chen, Y.H.; Kong, G.Q.; Chen, L.; Chen, G. Pile-soil stress ratio and settlement of in-situ shallow solidification-combined pipe-pile composite foundation under embankment load. *Rock Soil Mech.* **2022**, *43*, 688–696.
2. Xing, H.F.; Zhao, H.W.; Ye, G.B.; Xu, C. Analysis of engineering characteristics of PHC pipe piles. *Chin. J. Geotech. Eng.* **2009**, *31*, 36–39.
3. Luo, C.L.; He, J.C.; Ding, J.; Xia, Y.M. Numerical analysis on liquefaction properties and driving penetration of vibrating pile. *J. Guangxi Univ. Nat. Sci. Ed.* **2011**, *36*, 923–929.
4. Lei, H.Y.; Li, X.; Lu, P.Y.; Huo, H.F. Field test and numerical simulation of squeezing effect of pipe pile. *Rock Soil Mech.* **2012**, *33*, 1006–1012.

5. Xie, Y.J.; Wang, H.Z.; Zhu, H.H. Soil plugging effect of PHC pipe pile during driving into soft clay. *Rock Soil Mech.* **2009**, *30*, 1671–1675.
6. Xing, H.F.; Zhao, H.W.; Xu, C.; Ye, G.B. Dring effect of PHC pipe piles. *Chin. J. Geotech. Eng.* **2009**, *31*, 1208–1212.
7. Yu, X.; Zhao, H.Q. The finite element analysis of large diameter PHC pipe pile soil plug effect. *Shanxi Archit.* **2014**, *40*, 69–71.
8. Chen, L.Z.; Gao, F.; Song, C.Y.; Cai, Z.H. Monitoring extrusion effects in soft clay ground caused by statically piling. *J. Shanghai Jiao Tong Univ.* **2003**, *37*, 1910–1915.
9. Liu, J.W; Wang, L.Z; Zhu, N.; Zhang, C.W.; Zhao, G.X. Large-scale model test on installation characteristics of open-ended pipe pile. *Chin. J. Eng.* **2019**, *41*, 269–277.
10. Ko, J.; Jeong, S.; Lee, J.K. Large deformation fe analysis of driven steel pipe piles with soil plugging. *Comput. Geotech.* **2016**, *71*, 82–97. [CrossRef]
11. Zhan, Y.X.; Yao, H.L.; Dong, Q.P.; He, D.P. Study of process of open-ended pipe pile driven into sand soil by particle flow simuation. *Rock Soil Mech.* **2013**, *34*, 283–289.
12. Tang, B.; Zhou, Y.J.; Lv, G.S. Model expermental investigation on plugging effect of open pile in Zhanjiang group structal clay. *Sci. Technol. Eng.* **2017**, *17*, 117–123.
13. Leane, B.M.; Gavin, F.G. Base resistance of jacFed pipe piles in sand. *J. Geotech. Geoenviron. Eng.* **2001**, *127*, 473–480. [CrossRef]
14. Wang, T.; Xue, H.; Wu, R. Mechanism of soil plug for jacked pipe pile in clay. *Rock Soil Mech.* **2018**, *39*, 4335–4341, 4350.
15. Doherty, P.; Gavin, F. Shaft capacity of open-ended piles in clay. *J. Geotech. Geoenviron. Eng.* **2011**, *137*, 1090–1102. [CrossRef]
16. Gavin, F.; Barry, M.L. The shaft capacity of pipe piles in sand. *Can. Geotech. J.* **2011**, *40*, 36–45. [CrossRef]
17. Thongmunee, S.; Matsumoto, T.; Kobayashi, S.I.; Ken, K. Experimental and Numerical Studies on Push-Up Load Tests for Sand Plugs in a Steel Pipe Pile. *Soils Found.* **2011**, *51*, 959–974. [CrossRef]
18. Mohammed, Y.; Fattah; Wissam, H.; Soudani, A.; Maher, O. Estimation of bearing capacity of open-ended model piles in sand. *Arab. J. Geosci.* **2016**, *9*, 242.
19. Mohammed, Y.; Fattah; Wissam, H.S.; Soudani, A. Bearing capacity of open-ended pipe piles with restricted soil plug. *Ships Offshore Struct.* **2015**, *11*, 501–516.
20. Zhang, G.J.; Guo, G.L.; Yu, C.X.; Liu, S.Z. Application of rapid photogrammetry system in the deformation observation of bridge. *Highway* **2017**, *62*, 193–197.
21. Yu, C.X.; Zhang, G.J.; Zhao, Y.Q.; Liu, X.D.; Ding, X.H.; Zhao, T.L. Bridge monitoring and warning system based on digital measurement technology. *J. Shandong Univ. (Eng. Sci.)* **2020**, *50*, 115–122.
22. Xu, F.; Yu, C.; Huang, G.; Liu, Y. The Monitor of Steel Structure Bend Deformation Based on Digital Photogrammetry. *Geomat. Inf. Sci. Wuhan Univ.* **2001**, *26*, 256–260.
23. Zhang, G.J.; Yu, C.X.; Guo, G.L. Application of digital close-range photogrammetry in the deformation observation of check gate. *J. Shandong Univ. (Eng. Sci. Ed.)* **2017**, *47*, 46–51.
24. Zhang, G.; Guo, G.; Li, L.; Yu, C. Study on the dynamic properties of a suspended bridge using monocular digital photography to monitor the bridge dynamic deformation. *J. Civ. Struct. Health Monit.* **2018**, *8*, 555–567. [CrossRef]
25. Zhang, G.; Guo, G.; Yu, C.; Li, L.; Hu, S.; Wang, X. Monitoring instantaneous dynamic displacements of masonry walls in seismic oscillation outdoors by monocular digital photography. *Math. Probl. Eng.* **2018**, *2018*, 1–15. [CrossRef]
26. Wu, L.Y. Research on Digital Photogrammetry Technology in Instantaneous Deformation Monitoring of Aircraft Structures. Master's Dissertation, Shandong Jianzhu University, Jinan, China, 2020.
27. Ge, Y.; Yu, C.; Zhao, T.; Liu, X. Real-Time Monitoring Deformation of Building Using Photography Dynamic Monitoring System. *Stavební Obz. Civ. Eng. J.* **2021**, *30*, 245–259. [CrossRef]
28. Ge, Y.; Yu, C.; Liu, X.; Wang, R. Monitoring dynamic deformation of communication tower using photography dynamic monitoring system. *IOP Conf. Ser. Earth Environ. Sci.* **2020**, *558*, 022061. [CrossRef]
29. Achour, K.; Benkhelif, M. A new approach to 3d reconstruction without camera calibration. *Pattern Recognit.* **2001**, *34*, 2467–2476. [CrossRef]
30. Brown, D.C. Close-range camera calibration. *Eng* **1971**, *8*, 855–866.
31. Bradski, G.R.; Kaehler, A. *Learning OpenCV—Computer Vision with the OpenCV Library: Software That Sees*; O'Reilly Media, Inc.: Sebastopol, CA, USA, 2008; pp. 154–159.
32. Tsai, R.Y. A versatile camera calibration technique for high-accuracy 3d machine vision metrology using off the shelf tv cameras and lenses. *IEEE J. Robot. Autom.* **1987**, *3*, 323–344. [CrossRef]
33. Zhang, Z. A flexible new technique for camera calibration. *IEEE Trans. Pattern Anal. Mach. Intell.* **2000**, *22*, 1330–1334. [CrossRef]
34. Zhang, G.J.; Yu, C.X.; Guo, G.L.; Gong, Y.Q. Monitoring Sluice Health in Vibration by Monocular Digital Photography and a Measurement Robot. *KSCE J. Civ. Eng.* **2019**, *23*, 2666–2678. [CrossRef]
35. Yu, C.; Zhang, G.; Ding, X.; Zhao, Y.; Guo, G. Monitoring dynamic deformation of shuttle steel shelves by digital photography. *Civ. Eng. J.* **2019**, *27*, 136–150. [CrossRef]
36. Gao, M. A field investigation and analysis of a large pipe pile under static and dynamic lateral loadings. *Acta Entomol. Sin.* **1986**, *29*, 272–282.
37. Wu, W.; El Naggar, M.H.; Abdlrahem, M.; Mei, G.; Wang, K. New interaction model for vertical dynamic response of pipe piles considering soil plug effect. *Can. Geotech. J.* **2017**, *54*, 987–1001. [CrossRef]

38. Zheng, C.; Luan, L.; Qin, H.; Zhou, H. Horizontal dynamic response of a combined loaded large-diameter pipe pile simulated by the timoshenko beam theory. *Int. J. Struct. Stab. Dyn.* **2020**, *20*, 18. [CrossRef]
39. Trung, N.T.; Kiyomiya, O.; Yoshida, M. The dynamic behavior of a steel pipe sheet pile foundation in a liquefied layer during an earthquake. *J. JSCE* **2014**, *2*, 16–135. [CrossRef]